

The Super-Puff WASP-193 b is On A Well-Aligned Orbit*

SAMUEL W. YEE ^{1,†} GUDMUNDUR STEFÁNSSON ² DANIEL THORNGREN ³ ANDY MONSON ⁴ JOEL D. HARTMAN ⁵
DAVID B. CHARBONNEAU ¹ JOHANNA K. TESKE ^{6,7} R. PAUL BUTLER ⁶ JEFFREY D. CRANE ⁷ DAVID OSIP,⁸ AND
STEPHEN A. SHECTMAN ⁷

¹*Center for Astrophysics | Harvard & Smithsonian, 60 Garden St, Cambridge, MA 02138, USA*

²*Anton Pannekoek Institute for Astronomy, University of Amsterdam, 904 Science Park, Amsterdam, 1098 XH*

³*Department of Physics & Astronomy, Johns Hopkins University, Baltimore, MD 21210, USA*

⁴*Steward Observatory, University of Arizona, 933 N. Cherry Ave., Tucson, AZ 85721*

⁵*Department of Astrophysical Sciences, Princeton University, 4 Ivy Lane, Princeton, NJ 08544, USA*

⁶*Earth and Planets Laboratory, Carnegie Institution for Science, 5241 Broad Branch Road, NW, Washington, DC 20015, USA*

⁷*The Observatories of the Carnegie Institution for Science, 813 Santa Barbara Street, Pasadena, CA 91101, USA*

⁸*Las Campanas Observatory, Carnegie Institution for Science, Colina el Pino, Casilla 601, La Serena, Chile*

ABSTRACT

The “super-puffs” are a population of planets that have masses comparable to that of Neptune but radii similar to Jupiter, leading to extremely low bulk densities ($\rho_p \lesssim 0.2 \text{ g cm}^{-3}$) that are not easily explained by standard core accretion models. Interestingly, several of these super-puffs are found in orbits significantly misaligned with their host stars’ spin axes, indicating past dynamical excitation that may be connected to their low densities. Here, we present new Magellan/PFS RV measurements of WASP-193, a late F star hosting one of the least dense transiting planets known to date ($M_p = 0.112^{+0.029}_{-0.034} M_J$, $R_p = 1.319^{+0.056}_{-0.048} R_J$, $\rho_p = 0.060 \pm 0.019 \text{ g cm}^{-3}$). We refine the bulk properties of WASP-193 b and use interior structure models to determine that the planet can be explained if it consists of roughly equal amounts of metals and H/He, with a metal fraction of $Z = 0.42$. The planet is likely substantially re-inflated due to its host star’s evolution, and expected to be actively undergoing mass loss. We also measure the projected stellar obliquity using the Rossiter-McLaughlin effect, finding that WASP-193 b is on an orbit well-aligned with the stellar equator, with $\lambda = 17^{+17}_{-16}$ degrees. WASP-193 b is the first Jupiter-sized super-puff on a relatively well-aligned orbit, suggesting a diversity of formation pathways for this population of planets.

Keywords: Exoplanets (498), Hot Jupiters (753), Radial velocity (1332)

1. INTRODUCTION

Astronomical objects with sizes similar to that of Jupiter span several orders of magnitude in mass, ranging from gas giant planets to small stars. The least massive of these are the “super-puffs”, extrasolar planets with masses between that of Neptune and Saturn $20 M_\oplus \leq M_p \leq 100 M_\oplus$, corresponding to bulk densities of $\rho_p \lesssim 0.2 \text{ g cm}^{-3}$.

These extremely low density planets are not easily explained by standard core accretion models (Pollack et al. 1996), as their cores are thought to be susceptible to run-

away gas accretion, which would leave them with much larger gas envelopes and greater overall mass. These planets may instead be the result of stalled or inefficient gas accretion (Lee & Chiang 2016; Lee 2019) leading to masses much smaller than that of the typical gas giant. Such objects may also be physically inflated due to tidal dissipation in the planet’s interior (Millholland et al. 2020), or their observed radii may be larger than expected due to dusty outflows (Wang & Dai 2019).

Recent JWST transmission spectroscopy observations of WASP-107 b indeed suggest a higher than expected internal heat flux (Welbanks et al. 2024), consistent with planet inflation due to heating by tidal dissipation. Based on transit observations in the metastable He 10830 line, studies have also found that some of these

* This paper includes data gathered with the 6.5 meter Magellan Telescopes located at Las Campanas Observatory, Chile

† 51 Pegasi b Fellow

Neptune-mass super-puffs are actively losing mass (e.g., Spake et al. 2018; Vissapragada et al. 2024).

Intriguingly, several of the lowest density Neptune-mass objects have been found to be on orbits severely misaligned with their host star’s spin axes (Fig 6). The three super-puff Neptunes with published obliquity measurements ($M_p < 100 M_\oplus$, $\rho_p < 0.2 \text{ g cm}^{-3}$ —WASP-107 b (Dai & Winn 2017; Rubenzahl et al. 2021), WASP-127 b (Allart et al. 2020), and KELT-11 b (Mounzer et al. 2022)—are all on polar or retrograde orbits. It has therefore been suggested that these planets are the outcomes of a formation pathway involving excitation onto a high-inclination, high-eccentricity orbit, followed by tidal circularization that may be continuing to the present day (e.g., Yu & Dai 2024). Such a formation history would naturally explain their unusually high inclinations and inflated radii.

WASP-193 b is a newly discovered transiting planet that is a member of the population of puffy Neptunes. The planet was first detected by the WASP survey and described in Barkaoui et al. (2024, hereafter B24). WASP-193 b orbits a slightly evolved ($6.8_{-2.4}^{+3.1}$ Gyr old) solar mass star every 6.25 days, and has an inflated planetary radius of $R_p = 1.3 R_J$. B24 used radial velocity measurements from the HARPS and CORALIE spectrographs to measure the mass of WASP-193 b and found that it has a bulk density of just $\rho_p = 0.06 \text{ g cm}^{-3}$, making it one of the least dense planets discovered to date.

In this paper, we present new spectroscopic and photometric observations of WASP-193 b, including in-transit measurements taken with the goal of measuring the alignment between the planet’s orbit and stellar spin axis through the Rossiter-McLaughlin effect. We describe the observations in Section 2, and our global re-characterization of the system in Section 3. We then discuss the implications of our measurements for the internal structure and formation history of WASP-193 b in Section 4, and summarize in Section 5.

2. OBSERVATIONS

2.1. PFS Spectroscopy

We observed the WASP-193 system with the Planet Finder Spectrograph (PFS; Crane et al. 2006, 2008, 2010), a high-resolution echelle spectrograph on the Magellan Clay telescope at Las Campanas Observatory in Chile. All observations were made using the $0.3 \times 2.5''$ slit through an iodine cell, in 3×3 binning mode. An additional high signal-to-noise template observation of WASP-193 was taken without the iodine cell and used to derive precise radial-velocities (RVs).

Table 1. PFS Radial Velocities for WASP-193

Obs. Midpoint	Relative RV	σ_{RV}	Exp. Time
BJD _{TDB}	[m s^{-1}]	[m s^{-1}]	[s]
2460300.84220	-5.39	6.99	600
2460333.83057	7.53	5.20	600
2460337.85463	-18.99	5.62	600
2460338.82387	-0.29	5.78	600
2460341.81969	2.59	5.22	600
2460367.53478	-14.13	6.87	900
2460367.54523	6.74	5.38	900
2460367.55428	0.00	6.91	600
2460367.56132	16.18	6.23	600
2460367.57589	44.94	5.60	600

NOTE—This table is published in its entirety in the machine-readable format. A portion is shown here for guidance regarding its form and content.

We obtained a sequence of spectroscopic observations during a transit of WASP-193 b on the night of 2024 Feb 27. Observations began at 00 42 UT, when the target was at airmass 1.9 and continued for 6.5 hours, covering the entirety of the 4.25 hr transit event and an out-of-transit baseline comprising 0.75 hr pre-ingress and 1.5 hr post-egress. A total of 36 exposures were taken, with the first two having an exposure time of 900 seconds and the remainder being 600 second exposures. Conditions were clear and stable throughout the sequence, with typical airmass-corrected seeing of $0''.6$ or better. The spectroscopic data were reduced and precise RVs extracted using a custom IDL pipeline described in Butler et al. (1996). The median instrumental RV precision achieved during the transit night was 5.5 m/s.

We also observed WASP-193 on 13 additional epochs between 2023 Dec 22 and 2024 Jun 02, with the goal of refining the spectroscopic orbit of WASP-193 b. These observations were taken in the same instrument configuration and with 600s exposure times. The PFS RV data are presented in Table 1.

2.2. Ground-Based Transit Photometry

In addition to the in-transit spectroscopic observations on 2024 Feb 27, we also obtained simultaneous timeseries photometry. We observed with the Three-hundred MilliMeter Telescope (TMMT; Monson et al. 2017) and the 305 mm Las Campanas Remote Observatory (LCRO) robotic telescope, both at Las Campanas Observatory in Chile, in I and g' bands respectively. We used AstroImageJ (Collins et al. 2017) to perform aper-

ture photometry and extract flux time series for WASP-193. However, we noted that the TMMT data were affected by systematics on timescales similar to the transit ingress and egress duration, resulting in poor constraints on the transit timing. As such, we only used the LCRO data in our final analysis. Both datasets, together with variables used to detrend the photometry during the transit fit, are available in machine-readable form as Data behind the Figure for Figure 4.

2.3. Archival Data

We made use of archival spectroscopic and photometric data in our analysis. B24 published RV measurements from the HARPS and CORALIE spectrographs. We included the HARPS RVs in our analysis but not the CORALIE measurements, given their low precision (median instrumental uncertainty $\sigma_{\text{RV,CORALIE}} = 34 \text{ m s}^{-1}$) relative to the planet’s RV semi-amplitude ($K \approx 15 \text{ m s}^{-1}$).

B24 also published several follow-up transit light-curves obtained from the TRAPPIST-S (Gillon et al. 2011) and SPECULOOS (Jehin et al. 2018) facilities, dating back to 2015. We jointly fit these data in our analysis to extend the baseline of the transit data and precisely determine the transit ephemeris.

WASP-193 was observed by NASA’s Transiting Exoplanet Survey Satellite (TESS; Ricker et al. 2015) in Sectors 9, 36, and 63, with the transits of WASP-193 b clearly detected in the TESS light curves. We obtained the 2-minute cadence light curves reduced by the TESS Science Processing Operations Center (SPOC; Jenkins et al. 2016) for sectors 36 and 63 from MAST (STScI 2021, 2023). These data were also previously analyzed by B24.

In TESS Sector 9, WASP-193 was not one of the targets selected for 2-minute cadence observations, and so was only observed in the 30-minute cadence full-frame images (FFIs). While the TESS Quick-Look Pipeline (QLP; Kunimoto et al. 2021) produced a light curve for this object, we found that the planet’s transit depth in this sector is inconsistent with the depth measured in the other TESS observations as well as with the ground-based transits presented by B24, potentially due to an incorrect dilution correction applied to the QLP light curve. We performed an independent extraction of a light curve using the procedures of the T16 project (Hartman et al. 2025), which performs image subtraction on the full frame images with the difference imaging pipeline originally developed for the Cluster Difference Imaging Photometric Survey (CDIPS; Bouma et al. 2019). As the transit depth measured from this light curve is consistent with the other data, we used this

Table 2. Catalog Astrometry and Photometry for WASP-193 System

	WASP-193A	WASP-193B
<i>Identifiers</i>		
Gaia DR3 ID	5453063823882876032	5453063828179326976
TIC ID	49043968	49043967
2MASS ID	J10572385-2959497	J10572353-2959491
WISE ID	J105723.80-295949.7	J105723.48-295951.1
<i>Astrometry</i>		
Parallax (mas) ^a	2.648 ± 0.015	2.624 ± 0.045
μ_α (mas/yr) ^a	-49.055 ± 0.012	-49.494 ± 0.038
μ_δ (mas/yr) ^a	1.506 ± 0.016	2.259 ± 0.049
RV (km/s) ^a	-2.78 ± 0.82	–
Ang. Sep. (″) ^b	–	4.25
Proj. Sep. (AU) ^b	–	1600
$\mathcal{R}_{\text{chance}}^b$	–	2.91×10^{-7}
<i>Photometry</i>		
G (mag) ^a	12.033 ± 0.003	15.936 ± 0.003
G_{BP} (mag) ^a	12.335 ± 0.003	16.70 ± 0.02
G_{RP} (mag) ^a	11.567 ± 0.004	14.926 ± 0.006
T (mag) ^c	11.634 ± 0.008	15.104 ± 0.007
J (mag) ^d	10.952	11.794
H (mag) ^d	10.810 ± 0.034	13.011 ± 0.053
K (mag) ^d	10.745 ± 0.035	12.804 ± 0.048
W1 (mag) ^e	10.640 ± 0.026	13.27 ± 0.19
W2 (mag) ^e	10.677 ± 0.026	13.18 ± 0.19
W3 (mag) ^e	10.491 ± 0.093	12.12

References—^aGaia DR3 (Brown et al. 2021; Riello et al. 2021; Lindgren et al. 2021; Katz et al. 2022); ^bWide stellar binary catalog from El-Badry et al. (2021); ^cTESS Input Catalog (Stassun et al. 2019); ^d2MASS (Cutri et al. 2003; Skrutskie et al. 2006); ^eWISE (Cutri 2012).

reduction of the TESS Sector 9 data in our analysis. This TESS light curve is provided in machine-readable form with Figure 1. We detrended all TESS photometry by fitting the out-of-transit continuum to a basis spline, using the `Keplerspline` code (Vanderburg & Johnson 2014; Shallue & Vanderburg 2018). We then clipped the detrended light curves to use only data taken within ± 1.5 transit durations of a transit event.

2.4. Stellar Companion

A search of archival survey data around WASP-193 revealed a faint, nearby star with a sky separation of $4''25$, also noted by B24. This star is identified in the *Gaia*

(Gaia Collaboration et al. 2022), 2MASS (Cutri et al. 2003; Skrutskie et al. 2006), and WISE (Cutri 2012) surveys, and we list its photometric and astrometric measurements in Table 2.¹ Given this star has nearly identical parallax and proper motion compared with WASP-193, the two components are almost certainly bound. Indeed, the pair of stars appears in the El-Badry et al. (2021) catalog of stellar binaries from Gaia EDR3, with a chance alignment statistic $\mathcal{R} = 2.9 \times 10^{-7}$, indicating a high probability of being a bound pair with a sky-projected separation of ≈ 1600 AU. In the rest of this manuscript, we refer to this secondary stellar component as WASP-193B.

3. ANALYSIS

We performed a detailed analysis of the new and archival data to characterize the WASP-193 system. We used the `SpecMatch-Synthetic` code to obtain stellar spectroscopic properties of the host star (§3.1). We fitted the broadband fluxes, transit photometry, and out-of-transit radial velocities with `EXOFASTv2` to retrieve the planetary bulk properties (§3.2). Finally, we analyzed the in-transit RVs for the RM effect with the `rmfit` code (§3.3).

3.1. Spectroscopic Stellar Properties

We derived spectroscopic stellar parameters for the planet host star WASP-193 by analyzing the high SNR, iodine-free template spectrum we obtained with PFS. We used the `SpecMatch-Synthetic` code (Petigura 2015), which compares the observed spectrum with the Coelho et al. (2005) library of synthetic spectra, finding the best matches. The code interpolates within the library stellar grid by taking linear combinations of the closest spectra to better match the target spectrum, and applies those coefficients to the grid properties to derive the final stellar parameters. During this process, the library spectra are convolved with a broadening kernel to account for line broadening due to macroturbulence, assuming the $T_{\text{eff}} - v_{\text{mac}}$ relation from Valenti & Fischer (2005), as well as stellar rotation, enabling a measurement of $v \sin i$.

We determined that the planet host WASP-193 has $T_{\text{eff}} = 6000 \pm 60$ K, $\log g = 4.02 \pm 0.08$ dex, $[\text{Fe}/\text{H}] = -0.12 \pm 0.06$ dex, and $v \sin i = 4.7 \pm 1.0$ km s⁻¹. These results are all consistent within 1- σ of the spectroscopic properties derived by B24 from an analysis of HARPS and CORALIE spectra. We used the spectroscopic $[\text{Fe}/\text{H}]$ measurement as a prior for our global `EXOFASTv2`

modelling (§3.2), and the $v \sin i$ measurement as a prior for our analysis of the Rossiter-McLaughlin effect (§3.3).

3.2. Global System Characterization

We used the `EXOFASTv2` code (Eastman et al. 2019) to self-consistently model the planet and stars in the WASP-193 system. To constrain the planet properties, we fitted the out-of-transit RVs from PFS and HARPS, allowing for an independent RV offset for each instrument. We parameterized the planet’s orbital eccentricity in terms of $\sqrt{e} \cos \omega$ and $\sqrt{e} \sin \omega$. We also fitted the TESS and ground-based transit light curves. While the TESS data are already corrected for dilution from nearby known stars within the same pixel, including from the secondary star WASP-193B, we allowed for an additional dilution term to account for potential uncertainties or errors in that correction. We placed a Gaussian prior on this parameter with a width equal to 10% of the existing correction. For the ground-based photometry, we simultaneously detrended the light curves while fitting the transit model, using an additive detrending model. The detrending vectors used were linear time, pixel position, and meridian flip for the LCRO photometry, while for the for the archival TRAPPIST-S and SPECULOOS data, we used the same variables as in B24.

In addition to modelling the planet, `EXOFASTv2` simultaneously characterizes the stellar properties of the host star by fitting the star’s observed spectral energy distribution (SED) with the bolometric correction tables derived from the MIST evolutionary models (Dotter 2016; Choi et al. 2016). This self-consistent approach incorporates the transit constraint on the stellar density and ensures the limb-darkening coefficients used in the transit model are consistent with the stellar properties, assuming a quadratic limb-darkening law and coefficients tabulated by Claret & Bloemen (2011); Claret (2017). We accounted for both stars in the system using an updated version of `EXOFASTv2` that allows fitting of a two-component SED. As input data, we fitted the broadband catalog photometry from Gaia, 2MASS, and WISE (Table 2). The 4''3 separation of the two stars is easily resolved by Gaia, but is close to the angular resolution limit of the 2MASS and WISE catalogs, so the fluxes reported for the secondary star in those catalogs may not be reliable. We therefore fit the Gaia photometry for the two stars individually, while for the 2MASS and WISE photometry, we summed the measured fluxes and modelled the two stars as blended in those bands. We excluded the 2MASS J -band flux in the fit due to a flag indicating poor data quality. We placed Gaussian priors on the parallax of the star from Gaia DR3 (Lindgren

¹ Gaia parallaxes have been corrected with the zero-point correction from Lindgren et al. (2021).

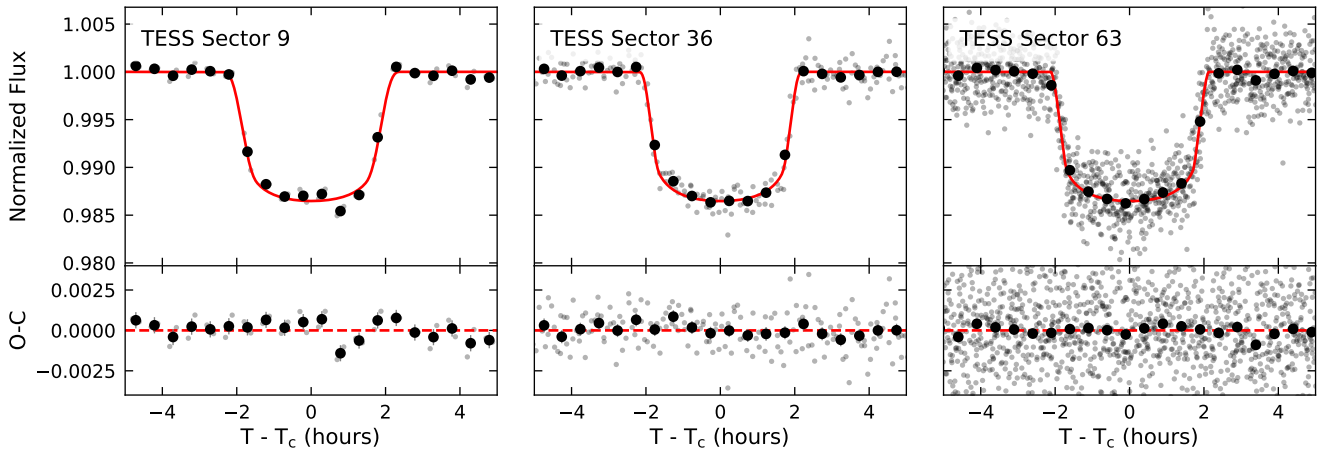


Figure 1. TESS light curves of WASP-193 from Sectors 9, 36, and 63 (left to right), phase-folded and clipped around the transit of WASP-193 b. Solid black points show measurements binned to 30 minute intervals. The red line shows the best-fitting transit model. The detrended TESS photometry used to create this figure are available in machine-readable form.

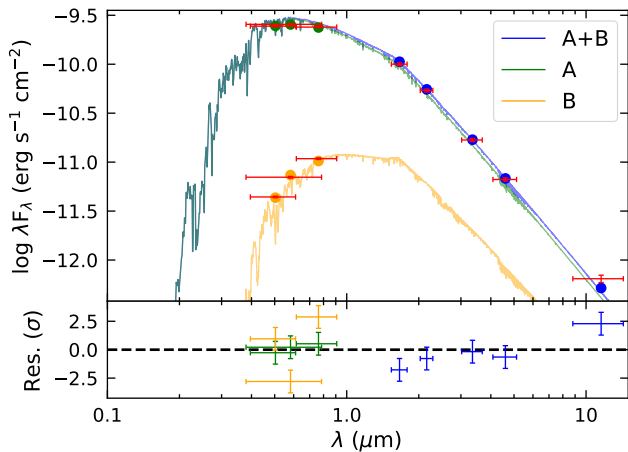


Figure 2. Modelled two-component Spectral Energy Distribution (SED) for the WASP-193AB system, based on the best-fitting stellar model from the EXOFASTv2 fit. The circles show the model broad-band averages, while the red crosses denote observed fluxes from the Gaia, 2MASS, and WISE catalogs. The horizontal error bars represent the filter bandwidths. The lower panel shows the differences between the observed and modelled fluxes, colored according to whether the observation represents the flux from WASP-193A (green), WASP-193B (yellow), or a blend of both (blue).

et al. 2021), $[\text{Fe}/\text{H}]$ based on our spectroscopic analysis, and an upper limit on the V-band extinction from the Schlafly & Finkbeiner (2011) dust maps. We required both stellar components to have the same distance, ex-

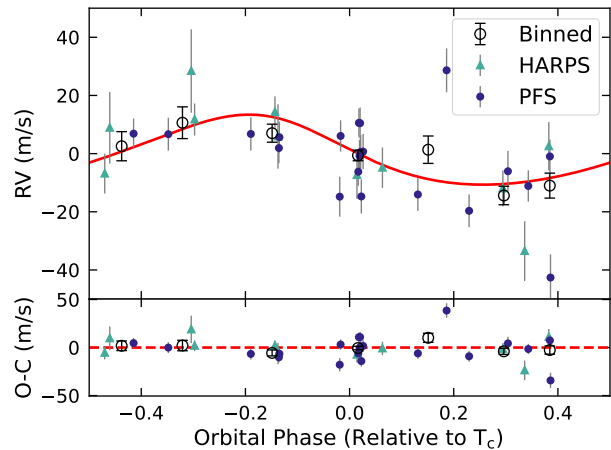


Figure 3. Observed RVs of WASP-193 from HARPS and PFS, phase-folded to the orbital period of WASP-193 b, excluding those measurements taken during the planet’s transit. A relative RV offset between the two instruments has been removed. The best-fitting RV model is plot as the red line, while open circles show the data binned by orbital phase.

tingtion, initial $[\text{Fe}/\text{H}]$ and age,² since they are likely a bound pair that formed together.

The best-fit stellar and planetary properties from our EXOFASTv2 analysis are presented in Table 3, while additional fit parameters, such as detrending coefficients, are reported in the Appendix in Table 5. Uncertain-

² To account for potential systematic errors in the MIST stellar models, we allowed stellar age of both stars to vary separately, but imposed a Gaussian prior on their age difference of width 0.1 Gyr.

Table 3. Median values and 68% Confidence Intervals for EXOFASTv2 fit of WASP-193

Parameter	Description	Value	
Stellar Parameters:		WASP-193A	WASP-193B
$M_\star (M_\odot)$	Stellar mass	$1.018^{+0.064}_{-0.062}$	0.594 ± 0.026
$R_\star (R_\odot)$	Stellar radius	$1.213^{+0.050}_{-0.042}$	$0.579^{+0.025}_{-0.026}$
$\log g_\star$ (cgs)	Stellar surface gravity	$4.280^{+0.042}_{-0.050}$	$4.686^{+0.030}_{-0.029}$
ρ_\star (g cm $^{-3}$)	Stellar density	0.81 ± 0.11	$4.31^{+0.51}_{-0.43}$
$L_\star (L_\odot)$	Stellar luminosity	$1.82^{+0.13}_{-0.12}$	0.0780 ± 0.0046
T_{eff} (K)	Stellar effective temperature	6080 ± 130	4007^{+70}_{-68}
[Fe/H] (dex)	Metallicity	$-0.108^{+0.055}_{-0.056}$	$-0.027^{+0.066}_{-0.065}$
[Fe/H] $_0$ (dex) a	Initial metallicity	$-0.035^{+0.051}_{-0.050}$	$-0.035^{+0.051}_{-0.050}$
Age (Gyr) a	Stellar age	$6.8^{+3.1}_{-2.4}$	$6.8^{+3.1}_{-2.4}$
EEP	Equal evolutionary phase	411^{+18}_{-28}	315^{+11}_{-13}
A_V (mag) a	Visual extinction	$0.109^{+0.062}_{-0.070}$	$0.109^{+0.062}_{-0.070}$
d (pc) a	Distance	$377.6^{+2.2}_{-2.1}$	$377.6^{+2.2}_{-2.1}$
Planet Parameters:		WASP-193A b	
P (days)	Period	6.2463475 ± 0.0000015	
T_c (BJD $_{\text{TDB}}$)	Time of conjunction	$2459243.31080 \pm 0.00024$	
R_P (R_J)	Planet radius	$1.319^{+0.056}_{-0.048}$	
M_P (M_J)	Planet mass	$0.112^{+0.029}_{-0.034}$	
$(R_P/R_\star)^2$	Planet-star area ratio	$0.01248^{+0.00028}_{-0.00027}$	
K (m/s)	RV semi-amplitude	$12.3^{+3.1}_{-3.6}$	
a (AU)	Semimajor axis	0.0668 ± 0.0014	
a/R_\star	Planet-star separation	$11.86^{+0.51}_{-0.58}$	
i (deg)	Inclination	$89.25^{+0.51}_{-0.54}$	
$b \equiv a \cos i/R_\star$	Transit impact parameter	$0.147^{+0.11}_{-0.099}$	
e	Eccentricity	$0.081^{+0.076}_{-0.055}$	
ω (deg)	Argument of periastron	42^{+84}_{-50}	
$\sqrt{e} \cos \omega$	Eccentricity vector	$0.12^{+0.22}_{-0.26}$	
$\sqrt{e} \sin \omega$	Eccentricity vector	$0.12^{+0.13}_{-0.16}$	
ρ_P (g cm $^{-3}$)	Planet density	0.060 ± 0.019	
$\log g_P$ (cgs)	Planet surface gravity	$2.20^{+0.11}_{-0.16}$	
T_{eq} (K)	Planet equilibrium temperature	1250^{+22}_{-21}	
$\langle F \rangle$ (10^9 erg s $^{-1}$ cm $^{-2}$)	Incident flux	$0.547^{+0.039}_{-0.036}$	
T_{14} (days)	Transit duration	$0.17733^{+0.00099}_{-0.00085}$	
τ (days)	Ingress/egress duration	$0.01821^{+0.00095}_{-0.00044}$	

a These parameters are linked for both stellar components.

ties in the parameters were determined by sampling the posterior distributions with a Differential Evolution-Monte Carlo Markov Chain (DE-MCMC) procedure in the EXOFASTv2 code. Figures 1 – 3 show the best-fitting transit, stellar SED, and RV models. We find that the primary stellar component, WASP-193A, is slightly evolved solar mass star ($M_\star = 1.018^{+0.064}_{-0.062} M_\odot$, $R_\star = 1.213^{+0.050}_{-0.042} R_\odot$), with stellar properties within 1- σ of those reported by B24. Meanwhile, the sec-

ondary star WASP-193B is a late K star with a mass of $M_\star = 0.594 \pm 0.026 M_\odot$ (Figure 2).

With the addition of new RV measurements from PFS, we obtain a smaller mass for the transiting planet WASP-193 b of $M_p = 0.112^{+0.029}_{-0.034} M_J$ (Figure 3), approximately 1- σ lower than the mass of $M_p = 0.139 \pm 0.029 M_J$ reported by B24. While these two results do not differ at a statistically significant level, we note that measurements of the RV semi-amplitude K tend to be

biased upward when the number of observations is small (Shen & Turner 2008; Piaulet et al. 2021), so the downward revision in mass is not unexpected.

We also find a smaller radius for WASP-193 b of $R_p = 1.319_{-0.048}^{+0.056} R_J$, $3\text{-}\sigma$ lower than the $R_p = 1.464 \pm 0.058 R_J$ from B24. This discrepancy may arise from differences in the treatment of limb-darkening between the two works, as the measurements of the transit depth from the TESS light curves are similar (this work: $1.38 \pm 0.03\%$; B24: $1.24 \pm 0.11\%$). Still, because both the mass and radius of WASP-193 b are smaller than previously thought, we find a bulk density of the planet of $\rho_P = 0.060 \pm 0.019 \text{ g cm}^{-3}$, similar to the B24 value, and WASP-193 b remains an extremely low-density super-puff planet.

One possible explanation for WASP-193 b’s inflated size is tidal heating from ongoing tidal circularization, as has been invoked to explain the low densities of similar super-puffs like WASP-107 b (Piaulet et al. 2021). Dissipation arising from a relatively small but finite eccentricity of order $e \sim 0.05$, would provide sufficient internal heating to significantly inflate such planets, given their low masses and assuming Neptune-like tidal quality factors of $Q_P \sim 10^4$ (e.g., Leconte et al. 2010; Welbanks et al. 2024). B24 reported that their data and analysis supported a slightly eccentric orbit for WASP-193 b, with $e = 0.056_{-0.040}^{+0.068}$. With our additional PFS RV data, we measure $e = 0.081_{-0.055}^{+0.076}$, with a 68% and 95% upper limits of $e < 0.12$ and $e < 0.24$ respectively, consistent with this idea. However, eccentricity measurements are subject to an upward bias when the true eccentricity is low (Lucy & Sweeney 1971). Using detailed simulations, Hara et al. (2019) estimated that the bias in eccentricity is $b_e \approx \sigma_{RV}/K/\sqrt{\pi/(N_{\text{obs}} - p)}$, where p is the number of free parameters. Based on the currently available data for WASP-193, the expected bias in the eccentricity could be as large as $b_e \sim 0.2$, indicating that nonzero eccentricity measurements up to 0.2 could be suspect. Continued RV monitoring of the system, or precise secondary eclipse timing measurements from facilities like JWST, would be needed to confirm any nonzero eccentricity. If WASP-193 b’s orbit is indeed eccentric, an additional explanation must be sought to understand how it retained that eccentricity given its expected short tidal circularization timescale of $\tau_{\text{circ}} \lesssim 0.2 \text{ Gyr}$ (Adams & Laughlin 2006), many times shorter than the system age.

3.3. Rossiter-McLaughlin Analysis

We measured the projected stellar obliquity, λ , by modelling the PFS RV timeseries from the night of 2024 Feb 27 with the `rmfit` code Stefánsson et al. (2022)³. `rmfit` models the Rossiter-McLaughlin (RM) anomaly using the formulae of Hirano et al. (2010, 2011), using the standard parameterization of the RM parameters in terms of λ and $v \sin i$. We placed Gaussian priors on the planet’s orbital parameters based on the output of our EXOFASTv2 analysis. We also used a Gaussian prior on $v \sin i$, from our `SpecMatch-Syn` analysis of the stellar spectrum (§3.1). We also repeated the RM analysis with an uninformative prior on $v \sin i$ and obtained consistent results, but elected to use the Gaussian prior, which helps eliminate a long tail toward high $v \sin i$ that is inconsistent with the spectroscopic line broadening measurement. For the remaining parameters, we used uninformative priors, and all priors are reported in Table 4.

`rmfit` first finds the maximum likelihood model parameters using a differential evolution global optimization algorithm (Storn & Price 1997) as implemented in `PyDE`.⁴ We then sampled the posterior probability distributions through an MCMC analysis using the `emcee` code (Goodman & Weare 2010; Foreman-Mackey et al. 2013) to determine uncertainties on those parameters. We confirmed the chains were well-mixed using the criteria for the Gelman-Rubin statistic, $GR < 1.01$ (Gelman & Rubin 1992), and that the total chain length was > 50 times the mean autocorrelation length. The median and 67% confidence intervals for each parameter are reported in Table 4.

The RV data, contemporaneous photometry and best-fitting model are plotted in Figure 4. We detect the RM anomaly at very high significance, with an RM semi-amplitude of $\approx 50 \text{ m s}^{-1}$, almost three times larger than the amplitude of the stellar reflex motion from the orbiting planet. We find that WASP-193 b has a projected stellar obliquity of $\lambda = 17_{-16}^{+17}^\circ$, consistent with a planetary orbit well-aligned with the stellar spin equator.

4. DISCUSSION

4.1. Interior Structure of WASP-193 b

With a bulk density of $\rho = 0.060 \pm 0.019 \text{ g cm}^{-3}$, WASP-193 b is one of the least dense exoplanets known to date (Figure 6). Only the Kepler-51 system (Masuda 2014) hosts planets with lower densities, although as a compact multi-planet system containing lower mass planets, Kepler-51 appears qualitatively different from

³ <https://github.com/gummiks/rmfit>

⁴ <https://github.com/hpparvi/PyDE>

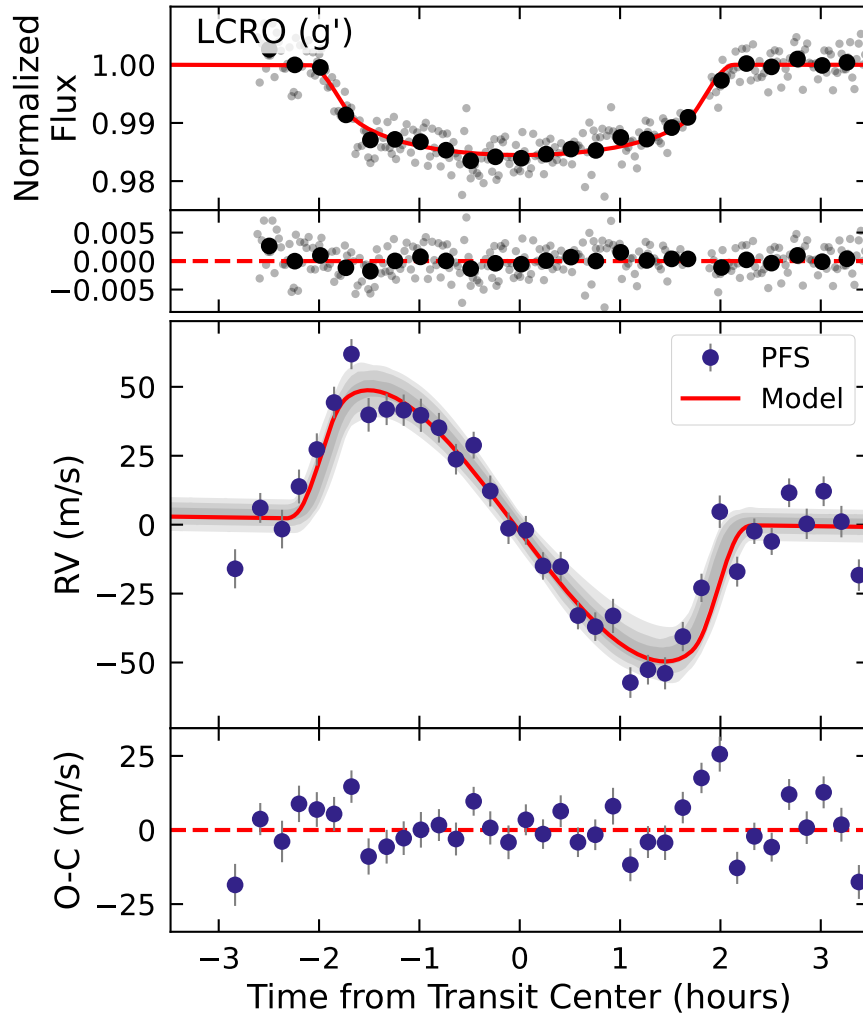


Figure 4. In-transit photometric data from LCRO (top) and PFS RV measurements (bottom) for WASP-193, taken on the night of 2024 Feb 27. The LCRO photometry was fit as part of our global EXOFASTv2 analysis, and the transit constraints used as priors for the `rmfit` analysis of the RM effect seen in the PFS RVs. The red line shows the best-fitting model, and the gray shaded regions in the lower panel show the 1, 2, and 3- σ confidence intervals for the RM model. The data behind this figure is available in machine-readable form.

the systems containing isolated puffy Neptunes like WASP-107, TOI-1420, and WASP-193.

We applied interior structure models to WASP-193 b to interpret its radius given its mass, equilibrium temperature, and age. The planet has $T_{\text{eq}} = 1250_{-21}^{+22}$ K, so we use the models of [Thorngren & Fortney \(2018\)](#) to account for the hot Jupiter inflation effect seen in objects with $T_{\text{eq}} \gtrsim 1000$ K (Figure 5). For the T_{eq} of WASP-193 b, the models call for approximately 1.1% of the incident flux to be added as internal heating. Accounting for the uncertainties in this value as well as the observed planet properties, we find that we can reproduce the mass and radius of the planet if it has a bulk metal content of $Z_p = 0.42 \pm 0.08$. Note that the quoted uncertainties do not include theoretical uncertainties on the modeling inputs, such as the H/He equation of state

and the distribution of metals between the core and envelope. [Thorngren et al. \(2016\)](#) evaluated the potential effect of these uncertainties on the inferred properties and found that they may result in 10–20% deviations, primarily arising from the choice of equation of state.

This inferred bulk metallicity is consistent with the predicted $Z_p = 0.42_{-0.19}^{+0.34}$ from the mass-metallicity relation of [Thorngren et al. \(2016\)](#), although at these low masses, the distribution of predictions is broad. Still, these models are able to explain the mass and radius of WASP-193 b with a physically plausible interior structure and the “standard” hot Jupiter inflation, without needing to invoke an additional source of heat, for example due to tides. The large size of WASP-193 b is therefore consistent with the overall hot Jupiter population,

Table 4. Priors and Fit Results for RM Analysis

Parameter	Description	Prior	Posterior
T_c (BJD _{TDB})	Transit midpoint	$\mathcal{N}(2460367.65298, 0.00037)$	$2460367.65277 \pm 0.00036$
P (days)	Orbital period	$\mathcal{N}(6.2463475, 0.0000015)$	6.2463475 ± 0.0000015
λ (deg)	Sky-projected obliquity	$\mathcal{U}(-180.0, 180.0)$	17^{+17}_{-16}
$v \sin i_*$ (km/s)	Projected stellar rotation velocity	$\mathcal{N}(4.7, 1.0)$	$4.84^{+0.42}_{-0.35}$
i (deg)	Transit inclination	$\mathcal{N}(89.25, 0.53)$	$89.37^{+0.36}_{-0.45}$
R_p/R_*	Planet-star radius ratio	$\mathcal{N}(0.1117, 0.0012)$	0.1117 ± 0.0012
a/R_*	Scaled semimajor axis	$\mathcal{N}(11.86, 0.54)$	$11.59^{+0.40}_{-0.42}$
u_1	Linear limb-darkening coefficient	$\mathcal{U}(0.0, 1.0)$	$0.38^{+0.29}_{-0.25}$
u_2	Quadratic limb-darkening coefficient	$\mathcal{U}(0.0, 1.0)$	$0.43^{+0.34}_{-0.30}$
$\sqrt{e} \cos \omega$	Eccentricity vector	$\mathcal{N}(0.12, 0.24)$	$0.07^{+0.16}_{-0.19}$
$\sqrt{e} \sin \omega$	Eccentricity vector	$\mathcal{N}(0.12, 0.15)$	$0.09^{+0.12}_{-0.13}$
β (km/s)	Intrinsic stellar line width	$\mathcal{N}(4.6, 1.0)$	$4.55^{+0.96}_{-0.94}$
K (m/s)	RV semi-amplitude	$\mathcal{N}(12.3, 3.4)$	12.2 ± 3.3
γ (km/s)	PFS RV offset	$\mathcal{N}(-0.2, 3.1)$	0.0 ± 2.0
σ_{RV} (m/s)	PFS RV jitter	$\mathcal{U}(0.0, 100.0)$	$7.8^{+1.6}_{-1.5}$

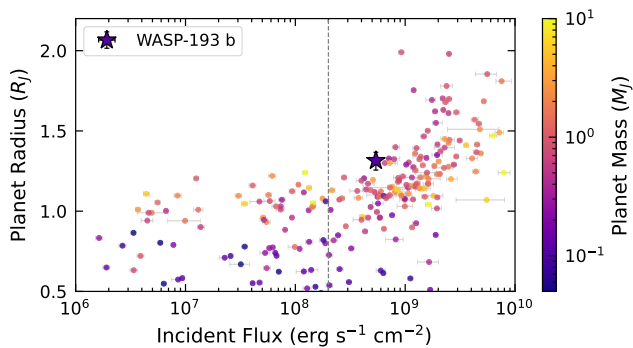


Figure 5. Radii of known transiting exoplanets as a function of incident flux, showing the onset of the hot Jupiter anomalous inflation at $\sim 2 \times 10^8 \text{ erg s}^{-1} \text{ cm}^{-2}$ (vertical dashed line). Points are colored according to mass, and only planets with masses measured to 33% and radii to 20% are shown here. WASP-193 b is marked with a star. Data for literature planets are taken from the NASA Exoplanet Archive PSCompPars table (NASA Exoplanet Archive 2022).

once its low mass and high equilibrium temperature are accounted for.

The inferred metal content implies an upper limit on the planet’s core mass $M_{\text{core}} < M_p Z_p = 15.0^{+7.4}_{-6.5} M_{\oplus}$, sufficiently large that standard core accretion theory predicts that it should have undergone runaway gas accretion. Thus, WASP-193 b appears to fall in the interesting and uncommon mass regime of giant planets that have avoided the fate of accreting a massive gas envelope, having roughly equal quantities of metals and H/He.

Of particular interest from an interior structure perspective is the fact that the host star appears to be near the end of its main sequence lifetime. MIST stellar evolution tracks (Choi et al. 2016) indicate that WASP-193 has increased its total luminosity by a factor of ~ 2 over the main sequence; as such, the planet spent most of its lifetime at an equilibrium temperature closer to 1000 K. As this is approximately the turn-on temperature for hot Jupiter inflation, the planet has had the opportunity to reflate (Lopez & Fortney 2016), as we estimate the same planet would have been 20-30% smaller at 1000 K, based on the minimum radius reached while evolving our planet interior structure models. Further, the present-day radius of $1.319^{+0.056}_{-0.048} R_J$ is clearly inflated, so this planet is a valuable addition to the small list of planets showing direct signs of reflation, along side such planets as K2-132 b and K2-97 b (Grunblatt et al. 2017).

The low bulk density of WASP-193 b has an additional important implication; the planet is likely to be very vulnerable to runaway XUV-driven mass loss (see e.g. Thorngren et al. 2023). The XUV-luminosity tracks of Johnstone et al. (2021) predict that even at the star’s advanced age, it is bombarding the planet with an XUV flux of $\sim 3000 \text{ erg s}^{-1} \text{ cm}^{-2}$. Combined with the outflow models of Caldiroli et al. (2022), we estimate a present-day mass loss rate $3.3 M_{\oplus} / \text{Gyr}$. The star will likely have had an XUV luminosity an order of magnitude higher in its first Gyr of life, so we expect that the planet has likely lost a substantial portion of its mass

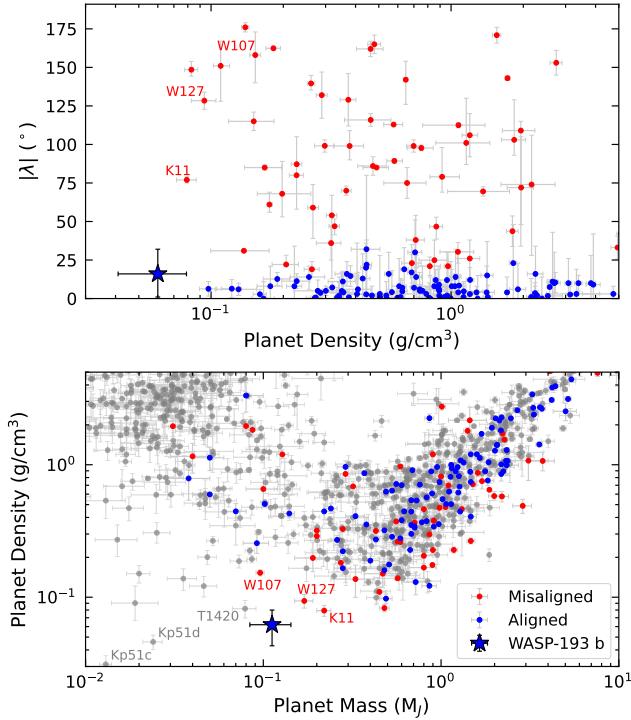


Figure 6. **Top:** Planets with measured projected stellar obliquity, as a function of bulk density. WASP-193 b is the least dense planet with such a measurement, and is marked with a star. Planets with measured obliquities are shown in red if they are consistent with significant misalignment with their host star’s spin (λ at least 1σ greater than 10°); and in blue for well-aligned orbits (aligned to better than 10° , roughly the scale at which our solar system is aligned). **Bottom:** Masses and densities of known transiting exoplanets. Objects with obliquity measurements are colored as in the top panel; those without such measurements are shown in gray. The other known super-puffs are labelled (WASP-107 b: W107; WASP-127 b: W127; KELT-11 b: K11; TOI-1420 b: T1420; Kepler-51 c/d: Kp51c/d). Of these, only W107, W127, and K11 have obliquity measurements and all show significant misalignments. In both panels, we use the same quality cuts on mass and radius measurements as in Figure 5. Mass and density data from the NASA Exoplanet Archive, while obliquity measurements are as compiled by Albrecht et al. (2022) and Knudstrup et al. (2024).

since formation, perhaps explaining its unusually high core-to-envelope ratio.

On the other hand, if the planet arrived more recently, such as through high-eccentricity migration (see Sec. 4.2), the planet may not have lost as much mass as if it had always been on its present orbit. The interaction between reinflation and XUV-driven mass loss will also be important in determining the history of this planet, but that would be a substantial project outside the scope of this article. We suggest that future work on this planet begin with a measurement of the present-day

stellar XUV luminosity as well as a search for signs of mass loss in the Helium triplet line during transit.

4.2. Obliquity of WASP-193 b In Context

Understanding how and when WASP-193 b arrived at its present location would inform the interpretation of future mass loss measurements and whether the planet has lost a significant fraction of its gas mass. Interestingly, the three other Neptune-mass super-puffs, namely WASP-107 b (Rubenzahl et al. 2021), WASP-127 b (Al-lart et al. 2020), and KELT-11 b (Mounzer et al. 2022), all have significantly misaligned orbits consistent with being polar or even retrograde to the stellar spin axis (Figure 6). These observations are consistent with a dynamically excited migration history for those planets, perhaps involving eccentricity excitation via Kozai-Lidov oscillations followed by tidal circularization (e.g., Yu & Dai 2024).

In contrast to other super-puffs, WASP-193 b appears to be on a relatively well-aligned orbit. We can confidently exclude the possibility that WASP-193 has a projected stellar obliquity as high as the $75 - 150^\circ$ measured for those objects. While the true angle between the planet’s orbital normal and the stellar spin axis, ψ , is not determined from the current data, a large true obliquity is *a priori* unlikely (Fabrycky & Winn 2009). One question is whether this low obliquity is the result of tidal realignment between the stellar spin axis and the planetary orbit, as has been proposed to operate for cool ($T_{\text{eff}} \lesssim 6200 \text{ K}$) planet-hosting stars with large convective envelopes (e.g., Winn et al. 2010; Schlaufman 2010). Attia et al. (2023) proposed a tidal efficiency factor

$$\tau \equiv \frac{M_{\text{conv}}}{M_\star} \left(\frac{M_p}{M_\star} \right)^2 \left(\frac{a}{R_\star} \right)^{-6}; \quad (1)$$

finding that for $\tau \lesssim 10^{-15}$, significant spin-orbit misalignments are observed for planets even around cool stars. They therefore suggested $\tau \sim 10^{-15}$ as an approximate threshold for determining whether tidal realignment has operated. In the case of WASP-193 b, its low mass and wide orbit ($a/R_\star = 11.6$ given the current stellar radius) result in $\tau \approx 10^{-16}$, suggesting that its current low obliquity is unlikely to be due to post-formation realignment.

We found that the WASP-193 system does not have a large spin-orbit misalignment, unlike the other super-puffs. This measurement excludes certain formation theories proposed to explain the preponderance of polar orbits particularly amongst Neptune-mass objects (Albrecht et al. 2021; Knudstrup et al. 2024; Espinoza-Retamal et al. 2024), such as disk-driven resonances that torque either the planet’s orbit (Petrovich et al. 2020)

or the stellar spin axis (Vick et al. 2023), which drive the stellar obliquity to high values. However, the precision of our measurement permits moderate misalignments of $\sim 30^\circ$, which would still be consistent with a high-eccentricity migration history driven by Kozai-Lidov oscillations. Using *Gaia* astrometry, we computed the angle between the sky-projected relative positions and velocities of the two stellar components (Tokovinin 1998; Tokovinin & Kiyaveva 2016; Dupuy et al. 2022), finding $\gamma = 43 \pm 3^\circ$. This indicates that the stellar binary orbit has a significant component in the sky-plane, in contrast to the orbit of the transiting planet, which is seen edge-on and would correspond to $\gamma = 0^\circ$. Thus, the M dwarf stellar companion WASP-193B is a potential inclined perturber that could drive such dynamics.

Alternatively, WASP-193 b may have formed without undergoing significant inclination excitation. The planet may have undergone early migration through a gas disk, or it may still have undergone high-eccentricity migration but without inclination excitation, for example through secular interactions with a coplanar distant perturber (Li et al. 2014; Petrovich 2015). In the first case, the planet is unlikely to have any significant orbital eccentricity, and may even have close-by, non-transiting companions, as is more common for warm Jupiters (Huang et al. 2016). We checked for Transit Timing Variations (TTVs) that may indicate the presence of nearby planets by fitting each observed transit independently, but found no evidence of any long-term variations above the typical ~ 1 – 2 minute precision on the individual mid-transit times. We do note that fitting the out-of-transit PFS RVs to a single Keplerian orbit required additional RV jitter larger than that expected for a star of this age (e.g., Luhn et al. 2020) as well as the excess noise measured over the hours-long timescale of the in-transit observations, so it is possible that the system does host additional short-period planets. Given the limited time baseline of current data, it is not possible to determine how exactly the WASP-193 system may have formed, and why it has such a low stellar obliquity compared to the other super-puffs. Continued RV monitoring or *Gaia* epoch astrometry could reveal additional distant planetary companions, or remanant eccentricity from formation that has not yet been tidally damped.

5. SUMMARY

We present new precise radial-velocity measurements of WASP-193 from Magellan/PFS, including an in-transit time series clearly detecting the Rossiter-

McLaughlin effect. We refine the radius and mass measurement of the transiting planet WASP-193 b, confirming its status as the lowest-density Neptune-mass planets known to date. Our interior structure models are able to reproduce the observed properties of WASP-193 b, given its high equilibrium temperature and accounting for the hot Jupiter radius inflation effect. These models also indicate that the planet must have an unusually high bulk metal mass fraction of $\gtrsim 40\%$, and is likely experiencing significant mass loss. Unlike other inflated Neptune-mass super-puffs, the orbit of WASP-193 b is comparatively well-aligned with its host star’s spin axis, and this alignment is likely to be primordial. This may suggest a diversity of formation pathways for these lowest density planets, or a common mechanism that produces both well-aligned and misaligned planets.

Continued RV monitoring of the system will improve constraints on WASP-193 b’s orbital eccentricity, placing limits on the level of tidal heating, as well as potentially detect additional planets in the system that may shed light on the planet’s formation. Given that the planet is likely losing mass, it is a prime target for detecting and measuring atmospheric outflows. Its large atmospheric scale height also means that WASP-193 b is a particularly favorable target for characterization of its atmosphere. Such observations would make for interesting comparisons with other puffy but polar Neptunes to connect planetary structure, mass loss, and migration history.

This paper is based on observations obtained from the Las Campanas Remote Observatory that is a partnership between Carnegie Observatories, The Astro-Physics Corporation, Howard Hedlund, Michael Long, Dave Jurasevich, and SSC Observatories.

The authors thank the anonymous referee for helpful comments that improved the quality and clarity of this work. S.W.Y. gratefully acknowledges support from the Heising-Simons Foundation. S.W.Y. thanks Shreyas Vissapragada, Jason Eastman, Sarah Millholland, and W. Brennom for helpful conversations. J.H. acknowledges support from NASA grant 80NSSC22K0409.

Facilities: Magellan:Clay (PFS)

Software: `astropy` (Astropy Collaboration et al. 2013, 2018); `EXOFASTv2` (Eastman et al. 2013; Eastman et al. 2019); `rmfit` (Stefánsson et al. 2022)

Table 5 contains additional fit parameters from our EXOFASTv2 analysis of the WASP-193 system.

Table 5. Additional fit parameters from EXOFASTv2 analysis of WASP-193

Parameter	Description	Value
RV Parameters:		
γ_{HARPS} (m/s)	Relative RV offset	$-3175.4^{+3.0}_{-3.1}$
$\sigma_{\text{jit,HARPS}}$ (m/s)	RV jitter	5.9 ± 5.9
γ_{PFS} (m/s)	Relative RV offset	-0.2 ± 3.1
$\sigma_{\text{jit,PFS}}$ (m/s)	RV jitter	$12.5^{+3.3}_{-2.6}$
Wavelength Parameters:		
δ_{B}	Transit depth	$0.01708^{+0.00062}_{-0.00058}$
$u_{1,\text{B}}$	Linear limb-darkening coeff	$0.554^{+0.044}_{-0.043}$
$u_{2,\text{B}}$	Quadratic limb-darkening coeff	$0.222^{+0.040}_{-0.041}$
δ_{BB}	Transit depth	$0.01460^{+0.00046}_{-0.00044}$
$u_{1,\text{BB}}$	Linear limb-darkening coeff	$0.300^{+0.043}_{-0.044}$
$u_{2,\text{BB}}$	Quadratic limb-darkening coeff	0.301 ± 0.048
$\delta_{\text{g}'}$	Transit depth	$0.01674^{+0.00057}_{-0.00054}$
$u_{1,\text{g}'}$	Linear limb-darkening coeff	0.523 ± 0.045
$u_{2,\text{g}'}$	Quadratic limb-darkening coeff	0.271 ± 0.050
$\delta_{\text{z}'}$	Transit depth	$0.01373^{+0.00036}_{-0.00035}$
$u_{1,\text{z}'}$	Linear limb-darkening coeff	0.187 ± 0.033
$u_{2,\text{z}'}$	Quadratic limb-darkening coeff	$0.276^{+0.034}_{-0.033}$
δ_{TESS}	Transit depth	$0.01420^{+0.00035}_{-0.00033}$
$u_{1,\text{TESS}}$	Linear limb-darkening coeff	$0.251^{+0.027}_{-0.026}$
$u_{2,\text{TESS}}$	Quadratic limb-darkening coeff	0.292 ± 0.028
Transit Parameters:		
$\sigma_{\text{TESS}_9}^2$	Added variance	$1.2^{+1.5}_{-1.1} \times 10^{-7}$
A_{D,TESS_9}	Added dilution	$0.057^{+0.019}_{-0.020}$
F_{0,TESS_9}	Baseline flux	1.00016 ± 0.00012
$\sigma_{\text{TESS}_{36}}^2$	Added variance	$-0.6^{+1.4}_{-1.3} \times 10^{-7}$
$A_{D,\text{TESS}_{36}}$	Added dilution	$0.057^{+0.019}_{-0.020}$
$F_{0,\text{TESS}_{36}}$	Baseline flux	1.000509 ± 0.000086
$\sigma_{\text{TESS}_{63}}^2$	Added variance	$-4.6^{+2.2}_{-2.1} \times 10^{-7}$
$A_{D,\text{TESS}_{63}}$	Added dilution	$0.057^{+0.019}_{-0.020}$
$F_{0,\text{TESS}_{63}}$	Baseline flux	$0.999877^{+0.000070}_{-0.000069}$
σ_{LCRO}^2	Added variance	$2.95^{+0.60}_{-0.54} \times 10^{-6}$
$F_{0,\text{LCRO}}$	Baseline flux	0.99128 ± 0.00021
$C_{0,\text{LCRO}}$	Detrending coefficient	0.00866 ± 0.00043
$C_{1,\text{LCRO}}$	Detrending coefficient	-0.00249 ± 0.00055
$\sigma_{\text{TRAPPIST}_1}^2$	Added variance	$1.007^{+0.086}_{-0.079} \times 10^{-5}$
$F_{0,\text{TRAPPIST}_1}$	Baseline flux	0.99673 ± 0.00020

Table 5 continued

Table 5 (*continued*)

Parameter	Description	Value
$C_{0,\text{TRAPPIST}_1}$	Detrending coefficient	-0.00016 ± 0.00035
$C_{1,\text{TRAPPIST}_1}$	Detrending coefficient	0.00229 ± 0.00059
$\sigma_{\text{TRAPPIST}_2}^2$	Added variance	$1.091_{-0.067}^{+0.071} \times 10^{-5}$
$F_{0,\text{TRAPPIST}_2}$	Baseline flux	1.00775 ± 0.00031
$C_{0,\text{TRAPPIST}_2}$	Detrending coefficient	-0.00008 ± 0.00041
$C_{1,\text{TRAPPIST}_2}$	Detrending coefficient	-0.00669 ± 0.00057
$\sigma_{\text{TRAPPIST}_3}^2$	Added variance	$6.02_{-0.83}^{+0.89} \times 10^{-6}$
$F_{0,\text{TRAPPIST}_3}$	Baseline flux	1.00066 ± 0.00028
$C_{0,\text{TRAPPIST}_3}$	Detrending coefficient	0.0032 ± 0.0017
$C_{1,\text{TRAPPIST}_3}$	Detrending coefficient	0.0054 ± 0.0018
$\sigma_{\text{TRAPPIST}_4}^2$	Added variance	$-2.75_{-0.11}^{+0.13} \times 10^{-5}$
$F_{0,\text{TRAPPIST}_4}$	Baseline flux	$0.99878_{-0.00033}^{+0.00034}$
$C_{0,\text{TRAPPIST}_4}$	Detrending coefficient	$0.00105_{-0.00083}^{+0.00082}$
$C_{1,\text{TRAPPIST}_4}$	Detrending coefficient	$0.00047_{-0.00100}^{+0.00098}$
$\sigma_{\text{SPECULOOS}}^2$	Added variance	$5.25_{-0.61}^{+0.66} \times 10^{-6}$
$F_{0,\text{SPECULOOS}}$	Baseline flux	0.99558 ± 0.00018
$C_{0,\text{SPECULOOS}}$	Detrending coefficient	0.01094 ± 0.00069
$C_{1,\text{SPECULOOS}}$	Detrending coefficient	-0.0219 ± 0.0013

NOTE—The transit parameters for TRAPPIST and SPECULOOS refer to the follow-up photometry obtained by B24 and re-fit in our analysis, using the same detrending parameters. The four TRAPPIST light curves are indexed in chronological order.

REFERENCES

- Adams, F. C., & Laughlin, G. 2006, *The Astrophysical Journal*, 649, 1004, doi: [10.1086/506145](https://doi.org/10.1086/506145)
- Albrecht, S. H., Dawson, R. I., & Winn, J. N. 2022, *Publications of the Astronomical Society of the Pacific*, 134, 082001, doi: [10.1088/1538-3873/ac6c09](https://doi.org/10.1088/1538-3873/ac6c09)
- Albrecht, S. H., Marcussen, M. L., Winn, J. N., Dawson, R. I., & Knudstrup, E. 2021, arXiv:2105.09327 [astro-ph]. <https://arxiv.org/abs/2105.09327>
- Allart, R., Pino, L., Lovis, C., et al. 2020, *A&A*, 644, A155, doi: [10.1051/0004-6361/202039234](https://doi.org/10.1051/0004-6361/202039234)
- Astropy Collaboration, Robitaille, T. P., Tollerud, E. J., et al. 2013, *A&A*, 558, A33, doi: [10.1051/0004-6361/201322068](https://doi.org/10.1051/0004-6361/201322068)
- Astropy Collaboration, Price-Whelan, A. M., Sipőcz, B. M., et al. 2018, *AJ*, 156, 123, doi: [10.3847/1538-3881/aabc4f](https://doi.org/10.3847/1538-3881/aabc4f)
- Attia, O., Bourrier, V., Delisle, J.-B., & Eggenberger, P. 2023, DREAM II. The Spin-Orbit Angle Distribution of Close-in Exoplanets under the Lens of Tides, arXiv, doi: [10.48550/arXiv.2305.00829](https://doi.org/10.48550/arXiv.2305.00829)
- Barkaoui, K., Pozuelos, F. J., Hellier, C., et al. 2024, *Nature Astronomy*, 8, doi: [10.1038/s41550-024-02259-y](https://doi.org/10.1038/s41550-024-02259-y)
- Bouma, L. G., Hartman, J. D., Bhatti, W., Winn, J. N., & Bakos, G. Á. 2019, *The Astrophysical Journal Supplement Series*, 245, 13, doi: [10.3847/1538-4365/ab4a7e](https://doi.org/10.3847/1538-4365/ab4a7e)
- Brown, A. G. A., Vallenari, A., Prusti, T., et al. 2021, *Astronomy & Astrophysics*, 649, A1, doi: [10.1051/0004-6361/202039657](https://doi.org/10.1051/0004-6361/202039657)
- Butler, R. P., Marcy, G. W., Williams, E., et al. 1996, *PASP*, 108, 500, doi: [10.1086/133755](https://doi.org/10.1086/133755)
- Caldiroli, A., Haardt, F., Gallo, E., et al. 2022, *A&A*, 663, A122, doi: [10.1051/0004-6361/202142763](https://doi.org/10.1051/0004-6361/202142763)

- Choi, J., Dotter, A., Conroy, C., et al. 2016, *The Astrophysical Journal*, 823, 102, doi: [10.3847/0004-637X/823/2/102](https://doi.org/10.3847/0004-637X/823/2/102)
- Claret, A. 2017, *Astronomy & Astrophysics*, 600, A30, doi: [10.1051/0004-6361/201629705](https://doi.org/10.1051/0004-6361/201629705)
- Claret, A., & Bloemen, S. 2011, *Astronomy & Astrophysics*, 529, A75, doi: [10.1051/0004-6361/201116451](https://doi.org/10.1051/0004-6361/201116451)
- Coelho, P., Barbuy, B., Meléndez, J., Schiavon, R. P., & Castilho, B. V. 2005, *A&A*, 443, 735, doi: [10.1051/0004-6361:20053511](https://doi.org/10.1051/0004-6361:20053511)
- Collins, K. A., Kielkopf, J. F., Stassun, K. G., & Hessman, F. V. 2017, *AJ*, 153, 77, doi: [10.3847/1538-3881/153/2/77](https://doi.org/10.3847/1538-3881/153/2/77)
- Crane, J. D., Shectman, S. A., & Butler, R. P. 2006, in *Society of Photo-Optical Instrumentation Engineers (SPIE) Conference Series*, Vol. 6269, Society of Photo-Optical Instrumentation Engineers (SPIE) Conference Series, ed. I. S. McLean & M. Iye, 626931, doi: [10.1117/12.672339](https://doi.org/10.1117/12.672339)
- Crane, J. D., Shectman, S. A., Butler, R. P., et al. 2010, in *Society of Photo-Optical Instrumentation Engineers (SPIE) Conference Series*, Vol. 7735, *Ground-based and Airborne Instrumentation for Astronomy III*, ed. I. S. McLean, S. K. Ramsay, & H. Takami, 773553, doi: [10.1117/12.857792](https://doi.org/10.1117/12.857792)
- Crane, J. D., Shectman, S. A., Butler, R. P., Thompson, I. B., & Burley, G. S. 2008, in *Society of Photo-Optical Instrumentation Engineers (SPIE) Conference Series*, Vol. 7014, *Ground-based and Airborne Instrumentation for Astronomy II*, ed. I. S. McLean & M. M. Casali, 701479, doi: [10.1117/12.789637](https://doi.org/10.1117/12.789637)
- Cutri, R. M., Skrutskie, M. F., van Dyk, S., et al. 2003, *VizieR Online Data Catalog*, II/246
- Cutri, R. M. e. 2012, *VizieR Online Data Catalog*, II/311
- Dai, F., & Winn, J. N. 2017, *AJ*, 153, 205, doi: [10.3847/1538-3881/aa65d1](https://doi.org/10.3847/1538-3881/aa65d1)
- Dotter, A. 2016, *The Astrophysical Journal Supplement Series*, 222, 8, doi: [10.3847/0067-0049/222/1/8](https://doi.org/10.3847/0067-0049/222/1/8)
- Dupuy, T. J., Kraus, A. L., Kratter, K. M., et al. 2022, *Monthly Notices of the Royal Astronomical Society*, 512, 648, doi: [10.1093/mnras/stac306](https://doi.org/10.1093/mnras/stac306)
- Eastman, J., Gaudi, B. S., & Agol, E. 2013, *Publications of the Astronomical Society of the Pacific*, 125, 83, doi: [10.1086/669497](https://doi.org/10.1086/669497)
- Eastman, J. D., Rodriguez, J. E., Agol, E., et al. 2019, arXiv e-prints, arXiv:1907.09480. <https://arxiv.org/abs/1907.09480>
- El-Badry, K., Rix, H.-W., & Heintz, T. M. 2021, *Monthly Notices of the Royal Astronomical Society*, 506, 2269, doi: [10.1093/mnras/stab323](https://doi.org/10.1093/mnras/stab323)
- Espinoza-Retamal, J. I., Stefánsson, G., Petrovich, C., et al. 2024, *The Astronomical Journal*, 168, doi: [10.3847/1538-3881/ad70b8](https://doi.org/10.3847/1538-3881/ad70b8)
- Fabrycky, D. C., & Winn, J. N. 2009, *The Astrophysical Journal*, 696, 1230, doi: [10.1088/0004-637X/696/2/1230](https://doi.org/10.1088/0004-637X/696/2/1230)
- Foreman-Mackey, D., Hogg, D. W., Lang, D., & Goodman, J. 2013, *PASP*, 125, 306, doi: [10.1086/670067](https://doi.org/10.1086/670067)
- Gaia Collaboration, Vallenari, A., Brown, A., Prusti, T., & et al. 2022, *Astronomy & Astrophysics*, doi: [10.1051/0004-6361/202243940](https://doi.org/10.1051/0004-6361/202243940)
- Gelman, A., & Rubin, D. B. 1992, *Statistical Science*, 7, 457, doi: [10.1214/ss/1177011136](https://doi.org/10.1214/ss/1177011136)
- Gillon, M., Jehin, E., Magain, P., et al. 2011, *EPJ Web of Conferences*, 11, 06002, doi: [10.1051/epjconf/20101106002](https://doi.org/10.1051/epjconf/20101106002)
- Goodman, J., & Weare, J. 2010, *Communications in Applied Mathematics and Computational Science*, 5, 65, doi: [10.2140/camcos.2010.5.65](https://doi.org/10.2140/camcos.2010.5.65)
- Grunblatt, S. K., Huber, D., Gaidos, E., et al. 2017, *AJ*, 154, 254, doi: [10.3847/1538-3881/aa932d](https://doi.org/10.3847/1538-3881/aa932d)
- Hara, N. C., Boué, G., Laskar, J., Delisle, J. B., & Unger, N. 2019, *Monthly Notices of the Royal Astronomical Society*, 489, 738, doi: [10.1093/mnras/stz1849](https://doi.org/10.1093/mnras/stz1849)
- Hartman, J., Bakos, G., Bouma, L. G., & Csabry, Z. 2025, *The T16 Project: Image Subtraction Light Curves from TESS Cycle 1 Full-Frame Images for Stars with T < 16*, arXiv, doi: [10.48550/arXiv.2502.13792](https://doi.org/10.48550/arXiv.2502.13792)
- Hirano, T., Suto, Y., Taruya, A., et al. 2010, *The Astrophysical Journal*, 709, 458, doi: [10.1088/0004-637X/709/1/458](https://doi.org/10.1088/0004-637X/709/1/458)
- Hirano, T., Suto, Y., Winn, J. N., et al. 2011, *The Astrophysical Journal*, 742, 69, doi: [10.1088/0004-637X/742/2/69](https://doi.org/10.1088/0004-637X/742/2/69)
- Huang, C., Wu, Y., & Triaud, A. H. M. J. 2016, *The Astrophysical Journal*, 825, 98, doi: [10.3847/0004-637X/825/2/98](https://doi.org/10.3847/0004-637X/825/2/98)
- Jehin, E., Gillon, M., Queloz, D., et al. 2018, *The Messenger*, 174, 2, doi: [10.18727/0722-6691/5105](https://doi.org/10.18727/0722-6691/5105)
- Jenkins, J. M., Twicken, J. D., McCauliff, S., et al. 2016, in *Software and Cyberinfrastructure for Astronomy IV*, Vol. 9913 (SPIE), 1232–1251, doi: [10.1117/12.2233418](https://doi.org/10.1117/12.2233418)
- Johnstone, C. P., Bartel, M., & Güdel, M. 2021, *A&A*, 649, A96, doi: [10.1051/0004-6361/202038407](https://doi.org/10.1051/0004-6361/202038407)
- Katz, D., Sartoretti, P., Guerrier, A., et al. 2022, *Gaia Data Release 3 Properties and Validation of the Radial Velocities*, arXiv, doi: [10.48550/arXiv.2206.05902](https://doi.org/10.48550/arXiv.2206.05902)
- Knudstrup, E., Albrecht, S. H., Winn, J. N., et al. 2024, *Obliquities of Exoplanet Host Stars: 19 New and Updated Measurements, and Trends in the Sample of 205 Measurements*, arXiv. <https://arxiv.org/abs/2408.09793>

- Kunimoto, M., Huang, C., Tey, E., et al. 2021, *Research Notes of the AAS*, 5, 234, doi: [10.3847/2515-5172/ac2ef0](https://doi.org/10.3847/2515-5172/ac2ef0)
- Leconte, J., Chabrier, G., Baraffe, I., & Levrard, B. 2010, *Astronomy and Astrophysics*, 516, A64, doi: [10.1051/0004-6361/201014337](https://doi.org/10.1051/0004-6361/201014337)
- Lee, E. J. 2019, *The Astrophysical Journal*, 878, 36, doi: [10.3847/1538-4357/ab1b40](https://doi.org/10.3847/1538-4357/ab1b40)
- Lee, E. J., & Chiang, E. 2016, *The Astrophysical Journal*, 817, 90, doi: [10.3847/0004-637X/817/2/90](https://doi.org/10.3847/0004-637X/817/2/90)
- Li, G., Naoz, S., Kocsis, B., & Loeb, A. 2014, *ApJ*, 785, 116, doi: [10.1088/0004-637X/785/2/116](https://doi.org/10.1088/0004-637X/785/2/116)
- Lindgren, L., Klioner, S. A., Hernández, J., et al. 2021, *Astronomy & Astrophysics*, 649, A2, doi: [10.1051/0004-6361/202039709](https://doi.org/10.1051/0004-6361/202039709)
- Lopez, E. D., & Fortney, J. J. 2016, *ApJ*, 818, 4, doi: [10.3847/0004-637X/818/1/4](https://doi.org/10.3847/0004-637X/818/1/4)
- Lucy, L. B., & Sweeney, M. A. 1971, *AJ*, 76, 544, doi: [10.1086/111159](https://doi.org/10.1086/111159)
- Luhn, J. K., Wright, J. T., & Isaacson, H. 2020, *The Astronomical Journal*, 159, 236, doi: [10.3847/1538-3881/ab775c](https://doi.org/10.3847/1538-3881/ab775c)
- Masuda, K. 2014, *The Astrophysical Journal*, 783, 53, doi: [10.1088/0004-637X/783/1/53](https://doi.org/10.1088/0004-637X/783/1/53)
- Millholland, S., Petigura, E., & Batygin, K. 2020, *The Astrophysical Journal*, 897, 7, doi: [10.3847/1538-4357/ab959c](https://doi.org/10.3847/1538-4357/ab959c)
- Monson, A. J., Beaton, R. L., Scowcroft, V., et al. 2017, *The Astronomical Journal*, 153, 96, doi: [10.3847/1538-3881/153/3/96](https://doi.org/10.3847/1538-3881/153/3/96)
- Mounzer, D., Lovis, C., Seidel, J. V., et al. 2022, *A&A*, 668, A1, doi: [10.1051/0004-6361/202243998](https://doi.org/10.1051/0004-6361/202243998)
- NASA Exoplanet Archive. 2022, *Planetary Systems Composite Parameters*, Version: 2022-02-14, NExScI-Caltech/IPAC, doi: [10.26133/NEA13](https://doi.org/10.26133/NEA13)
- Petigura, E. A. 2015, PhD thesis, University of California, Berkeley, United States
- Petrovich, C. 2015, *The Astrophysical Journal*, 805, 75, doi: [10.1088/0004-637X/805/1/75](https://doi.org/10.1088/0004-637X/805/1/75)
- Petrovich, C., Muñoz, D. J., Kratter, K. M., & Malhotra, R. 2020, *The Astrophysical Journal*, 902, doi: [10.3847/2041-8213/abb952](https://doi.org/10.3847/2041-8213/abb952)
- Piaulet, C., Benneke, B., Rubenzahl, R. A., et al. 2021, *The Astronomical Journal*, 161, 70, doi: [10.3847/1538-3881/abcd3c](https://doi.org/10.3847/1538-3881/abcd3c)
- Pollack, J. B., Hubickyj, O., Bodenheimer, P., et al. 1996, *Icarus*, 124, 62, doi: [10.1006/icar.1996.0190](https://doi.org/10.1006/icar.1996.0190)
- Ricker, G. R., Winn, J. N., Vanderspek, R., et al. 2015, *Journal of Astronomical Telescopes, Instruments, and Systems*, 1, 014003, doi: [10.1117/1.JATIS.1.1.014003](https://doi.org/10.1117/1.JATIS.1.1.014003)
- Riello, M., Angeli, F. D., Evans, D. W., et al. 2021, *Astronomy & Astrophysics*, 649, A3, doi: [10.1051/0004-6361/202039587](https://doi.org/10.1051/0004-6361/202039587)
- Rubenzahl, R. A., Dai, F., Howard, A. W., et al. 2021, *The Astronomical Journal*, 161, 119, doi: [10.3847/1538-3881/abd177](https://doi.org/10.3847/1538-3881/abd177)
- Schlafly, E. F., & Finkbeiner, D. P. 2011, *The Astrophysical Journal*, 737, 103, doi: [10.1088/0004-637X/737/2/103](https://doi.org/10.1088/0004-637X/737/2/103)
- Schlaufman, K. C. 2010, *The Astrophysical Journal*, 719, 602, doi: [10.1088/0004-637X/719/1/602](https://doi.org/10.1088/0004-637X/719/1/602)
- Shallue, C. J., & Vanderburg, A. 2018, *The Astronomical Journal*, 155, 94, doi: [10.3847/1538-3881/aa9e09](https://doi.org/10.3847/1538-3881/aa9e09)
- Shen, Y., & Turner, E. L. 2008, *The Astrophysical Journal*, 685, 553, doi: [10.1086/590548](https://doi.org/10.1086/590548)
- Skrutskie, M. F., Cutri, R. M., Stiening, R., et al. 2006, *AJ*, 131, 1163, doi: [10.1086/498708](https://doi.org/10.1086/498708)
- Spake, J. J., Sing, D. K., Evans, T. M., et al. 2018, *Nature*, 557, 68, doi: [10.1038/s41586-018-0067-5](https://doi.org/10.1038/s41586-018-0067-5)
- Stassun, K. G., Oelkers, R. J., Paegert, M., et al. 2019, *The Astronomical Journal*, 158, 138, doi: [10.3847/1538-3881/ab3467](https://doi.org/10.3847/1538-3881/ab3467)
- Stefánsson, G., Mahadevan, S., Petrovich, C., et al. 2022, *The Astrophysical Journal Letters*, 931, L15, doi: [10.3847/2041-8213/ac6e3c](https://doi.org/10.3847/2041-8213/ac6e3c)
- Storn, R., & Price, K. 1997, *Journal of Global Optimization*, 11, 341, doi: [10.1023/A:1008202821328](https://doi.org/10.1023/A:1008202821328)
- STScI. 2021, *TESS Light Curves: Sector 36*, STScI/MAST, doi: [10.17909/X4V7-XD29](https://doi.org/10.17909/X4V7-XD29)
- . 2023, *TESS Light Curves: Sector 63*, STScI/MAST, doi: [10.17909/RZV6-R679](https://doi.org/10.17909/RZV6-R679)
- Thorngren, D. P., & Fortney, J. J. 2018, *AJ*, 155, 214, doi: [10.3847/1538-3881/aaba13](https://doi.org/10.3847/1538-3881/aaba13)
- Thorngren, D. P., Fortney, J. J., Murray-Clay, R. A., & Lopez, E. D. 2016, *ApJ*, 831, 64, doi: [10.3847/0004-637X/831/1/64](https://doi.org/10.3847/0004-637X/831/1/64)
- Thorngren, D. P., Lee, E. J., & Lopez, E. D. 2023, *The Astrophysical Journal Letters*, 945, L36, doi: [10.3847/2041-8213/acbd35](https://doi.org/10.3847/2041-8213/acbd35)
- Tokovinin, A., & Kiyaveva, O. 2016, *Monthly Notices of the Royal Astronomical Society*, 456, 2070, doi: [10.1093/mnras/stv2825](https://doi.org/10.1093/mnras/stv2825)
- Tokovinin, A. A. 1998, *Astronomy Letters*, 24, 178
- Valenti, J. A., & Fischer, D. A. 2005, *The Astrophysical Journal Supplement Series*, 159, 141, doi: [10.1086/430500](https://doi.org/10.1086/430500)
- Vanderburg, A., & Johnson, J. A. 2014, *Publications of the Astronomical Society of the Pacific*, 126, 948, doi: [10.1086/678764](https://doi.org/10.1086/678764)
- Vick, M., Su, Y., & Lai, D. 2023, *ApJL*, 943, L13, doi: [10.3847/2041-8213/acaead](https://doi.org/10.3847/2041-8213/acaead)

- Vissapragada, S., Greklek-McKeon, M., Linssen, D., et al. 2024, *The Astronomical Journal*, 167, 199, doi: [10.3847/1538-3881/ad3241](https://doi.org/10.3847/1538-3881/ad3241)
- Wang, L., & Dai, F. 2019, *The Astrophysical Journal Letters*, 873, L1, doi: [10.3847/2041-8213/ab0653](https://doi.org/10.3847/2041-8213/ab0653)
- Welbanks, L., Bell, T. J., Beatty, T. G., et al. 2024, *Nature*, 1, doi: [10.1038/s41586-024-07514-w](https://doi.org/10.1038/s41586-024-07514-w)
- Winn, J. N., Fabrycky, D., Albrecht, S., & Johnson, J. A. 2010, *The Astrophysical Journal Letters*, 718, L145, doi: [10.1088/2041-8205/718/2/L145](https://doi.org/10.1088/2041-8205/718/2/L145)
- Yu, H., & Dai, F. 2024, *The Astrophysical Journal*, 972, doi: [10.3847/1538-4357/ad5ffb](https://doi.org/10.3847/1538-4357/ad5ffb)